The effect of a flight stream on subsonic turbulent jets

Igor A Maia, Guillaume Brès, Lutz Lesshafft, Peter Jordan

The effect of a flight stream on subsonic turbulent jets

Igor A. Maia[1] †, Guillaume Brès[2], Lutz Lesshafft[3] and Peter Jordan[1]

[1]Département Fluides, Thermique, Combustion, Institut PPrime, CNRS - Université de Poitiers - ENSMA, Poitiers, France

[2]Cascade Technologies Inc., Palo Alto, CA94303, USA

[3]Laboratoire d'Hydrodynamique, CNRS - Ecole Polytechnique, Palaiseau, France

(Received xx; revised xx; accepted xx)

This study concerns a turbulent jet at Mach number $M_j = 0.9$, subject to a uniform external flow stream at $M_f = 0.15$. We assess the mechanisms that underpin the reduction in fluctuation energy that is known to occur when a jet is surrounded by a flight stream. The analysis combines experimental and numerical databases, spectral proper orthogonal decomposition (SPOD) and linear modelling. The experiments involve Time-Resolved, Stereo PIV measurements at different cross-sections of the jet. A companion large-eddy simulation was performed with the same operating conditions using the "CharLES" solver by Cascade Technologies in order to obtain a complete and highly resolved 3D database. We show that the energy reduction is spread over a broad region of the frequency-wavenumber space and involves, apart from the known stabilization of the modal Kelvin-Helmholtz (KH) instability, the attenuation of flow structures associated with the non-modal Orr and lift-up mechanisms. Streaky structures, associated with helical azimuthal wavenumbers and very slow time scales, are the most strongly affected by the flight stream, in terms of energy attenuation and spatial distortion. The energy reductions are accompanied by a weakening of the low-rank behaviour of the jet dynamics revealed by previous studies. These trends are found to be consistent with results of a local linear model based on the modified mean flow in the flight stream case.

Key words: Turbulent jets, flight stream, linear instability mechanisms.

1. Introduction

Recent research on turbulent shear flows has been driven by a need to obtain simplified descriptions of flow dynamics that would make the Navier-Stokes system mathematically tractable. The existence of coherent structures motivates the development of such simplified models. Despite their widespread presence in turbulent flows (Hussain 1986), a precise definition of what constitutes a coherent structure is elusive. They are often associated with large-scale (with respect to typical turbulence integral scales) organised motion important for phenomena such as the redistribution of momentum and energy, drag in wall-bounded flows (Jiménez 2018) and sound radiation by jets (Jordan and Colonius 2013).

Coherent structures are easily identifiable in unstable laminar flows, where the exponential growth of small disturbances underpins transition to turbulence. In that case, they can be

† Email address for correspondence: igor.albuquerque.maia@univ-poitiers.fr

modelled as instability waves using linear stability theory, where linearisation is performed about the laminar base state. In the turbulent regime, organised motion often persists and early observations in mixing layers (Brown and Roshko 1974) and jets (Mollo-Christensen 1967) revealed a remarkable resemblance with linear instability mechanisms found at lower Reynolds numbers. However, in the turbulent jet, which is the object of study of the present work, these structures are less easily identifiable because of their low fluctuation energy and their stochastic space-time organisation. That is why early attempts to study the dynamics of coherent structures in jets were often done using an external periodic forcing, in order to raise their energy above the background level and enhance their organisation (Crow and Champagne 1971; Moore 1977; Hussain and Zaman 1980a,b, 1981; Petersen and Samet 1988).

More recently, there has been progress in the identification and modelling of coherent structures in unforced jets, thanks to progress in experimental techniques, the use of advanced signal processing approaches such as Proper Orthogonal Decomposition (POD) (Lumley 1967) and Spectral Proper Orthogonal Decomposition (SPOD) and linear mean-flow modelling. For instance, Kelvin-Helmholtz (KH) type wavepackets have been identified in the hydrodynamic pressure near-field (Suzuki and Colonius 2006; Gudmundsson and Colonius 2011; Breakey et al. 2017) and in the velocity field (Cavalieri et al. 2013; Jaunet et al. 2017) of unforced turbulent jets. The experimentally-educed wavepackets are found to be in good agreement with solutions to the Parabolised Stability Equations (PSE) in the initial jet region for the azimuthal wavenumbers $m = 0, 1, 2$ and frequencies in the range $0.3 \leqslant St \leqslant 1$, with St being the Strouhal number. Later, Sasaki et al. (2017) showed, using Large Eddy Simulation data, that agreement persists for Strouhal numbers as high as $St = 4$ for the axisymmetric and first three helical azimuthal wavenumbers.

The above studies show compelling evidence of modal convective instability mechanisms in jets. More recently, attention has turned to non-modal linear mechanisms such as the Orr (Orr 1907) and Lift-up (Brandt 2014) mechanisms, that give rise to different flow structures. These mechanisms, known to be important in the dynamics of wall-bounded flows (see the reviews by Jiménez (2018) and Brandt (2014)), have been identified in jets using resolvent analysis (Garnaud et al. 2013a; Jeun et al. 2016; Semeraro et al. 2016; Tissot et al. 2017; Schmidt et al. 2018; Lesshafft et al. 2019; Nogueira et al. 2019; Pickering et al. 2020). In the resolvent framework, nonlinear Reynolds stresses are treated as an endogenous forcing that drives a linear operator (McKeon and Sharma 2010). A singular-value decomposition of the resolvent operator breaks it into a set of forcing and response modes. The former provide a basis onto which the non-linear forcing terms are projected. These projections, when scaled by the corresponding singular-value, or gains, associated to each forcing mode, equal the projection of the flow response in the basis formed by the response modes. For the axisymmetric azimuthal wavenumber, $m = 0$, it has been shown (Garnaud et al. 2013a; Jeun et al. 2016; Semeraro et al. 2016; Tissot et al. 2017; Schmidt et al. 2018; Lesshafft et al. 2019) that in the frequency range $0.3 \leqslant St \leqslant 1$ there is a large gain separation between the leading singular response mode of the resolvent operator and the first suboptimal. This gain separation is accompanied by a spatial separation between the forcing and response modes. The forcing mode has spatial support in the vicinity of the nozzle lip, where the flow jet is most receptive, and is characterised by elongated structures tilted against the mean flow, in a behaviour typical of the Orr mechanism. The associated flow response has spatial support further downstream and is underpinned by KH wavepackets issuing from a shear instability. This spatial separation between forcing and reponse suggests that the fluctuating Reynolds stresses can be neglected in a large portion of the jet, at least as far as first-order, single-point statistics are concerned. This explains the success of linear homogeneous models in capturing the modal behaviour of the response. This dynamics, characterised by Orr-forcing and KH-

response also takes place at non-zero azimuthal wavenumbers, although with a less marked low-rank behaviour, i.e. smaller gain separation between optimal and suboptimal singular values (Garnaud et al. 2013a). For the axisymmetric mode, $m = 0$, at low frequencies, $St < 0.3$, the gain separation is also small, and the gain associated with the KH mode may become sub-optimal (Schmidt et al. 2018). The optimal mechanism is then characterised by Orr-like structures both in the forcing and in the response.

The lift-up effect in shear flows, on the other hand, occurs at non-zero azimuthal wavenumbers and very low frequencies (in the limit $St/m \to 0$). This mechanism is characterised by streamwise vortices, or rolls, that induce elongated streamwise velocity streaks (Brandt 2014). Such structures have been observed in jets in the works of Becker and Massaro (1968); Browand and Laufer (1975); Dimotakis et al. (1983); Yule (1978); Agüí and Hesselink (1988). Later, using POD reconstruction of flow snapshots measured with a rake of hot-wires, Citriniti and George (2000) showed that rolls and streaks are clearly present among the most energetic flow structures for azimithal wavenumbers up to $m = 6$. Jung et al. (2004) found that the peak energy of the streaks is shifted towards lower azimuthal modes with incresing streamwise distance, a result that was later confirmed by Pickering et al. (2020) using SPOD of a large-eddy simulation (LES) database. The works of Jiménez-González and Brancher (2017), Nogueira et al. (2019), Pickering et al. (2020) and Wang et al. (2021) provide a modelling framework that clarifies the mechanisms that give rise to these structures, observed in these various experiments. The distinction between different kinds of modal (KH) and non-modal (lift-up and Orr) mechanisms in the resolvent framework can be made via the gain spectrum and the shape of the forcing and response modes. Based on these features, Pickering et al. (2020) proposed a linear mechanism map, illustrating the relative dominance of the different mechanisms in different regions of the frequency-wavenumber spectrum. Other works have focused on modelling interactions between different types of flow structures using nonlinear models and studying what role these interactions might have in the generation of self-sustained turbulence in shear flows (see for example the works of Waleffe (1997); Moehlis and H. Faisst a (2004); Eckhardt and Mersmann (1999); Hall and Sherwin (2010); Chantry et al. (2017); Cavalieri (2021); Nogueira and Cavalieri (2021) to cite just a few).

1.1. *Jets with flight stream*

The focus of this work is jets subject to a uniform external flight stream. It is known that a flight stream modifies the mean flow development, producing a stretching of the potential core, reduction of the shear-layer thickness and a reduction of the associated radiated sound levels (Tanna and Morris 1977). Such mean-flow modifications have a stabilizing effect on the modal KH mechanism, as shown by Michalke and Hermann (1982) with an inviscid locally parallel stability analysis. More recently, Soares et al. (2020) extended the analysis by taking into account the jet mean-flow divergence in a PSE formulation. The results confirm a reduction in wavepacket growth rates with increasing flight stream velocity, followed by an increase in their convection velocity. The linear dynamics of axisymmetric wavepackets in the presence of a coflow have also been studied by Garnaud et al. (2013b) using a global resolvent analysis. The flow response modes (both in the near-field and the far-field) were found to be in good qualitative agreement with (nonlinear) flow data.

Most studies of the effect of flight stream on jets focused on sound-radiation aspects (Glahn et al. 1973; Cocking and Bryce 1975; Bushel 1975; Packman et al. 1975; Plumbee 1975; Bryce 1984; Morfey and Tester 1977; Vishwanathan and Czech 2011). In this work we characterise the effect of a flight stream on the turbulent flow field of a subsonic jet. As discussed above, there is now a well-documented body of work concerning modal and non-modal linear mechanisms in jets in "static" conditions. And although the effect of the flight

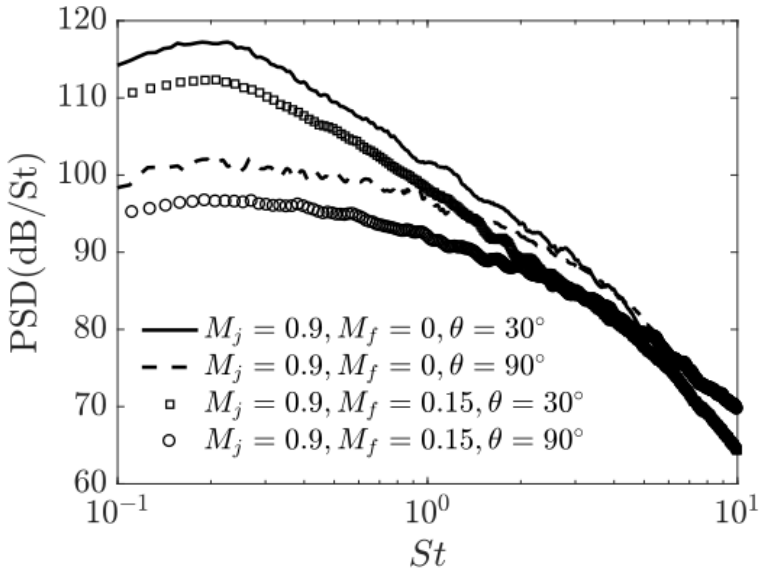

Figure 1: Power spectral densities (PSD) of pressure measured in the acoustic field of jets with and without flight stream at polar angles of $\theta = 30°$ and $\theta = 90°$ from the jet axis. *St* stands for Strouhal number.

stream on the KH instability has been studied (Michalke and Hermann 1982; Soares et al. 2020), to the best of our knowledge no studies so far have characterised the changes in non-modal instability mechanisms (Orr and Lift-up) in flight conditions. This is the main goal of the present work.

Figure 1 shows spectra of acoustic pressure measured at polar angles of $\theta = 30°$ and $\theta = 90°$ from the jet axis, in the setup described in §2. The flight stream is seen to produce an effect at both angles for a broad range of Strouhal numbers, as a consequence of changes to the turbulent field. At low frequencies and small angles from the jet axis, represented here by $\theta = 30°$, the main sound-producing mechanism is associated with axisymmetric ($m = 0$) jittering KH wavepackets (Cavalieri et al. 2011, 2012; Maia et al. 2019). At sideline, higher azimuthal wavenumbers become dominant, (Cavalieri et al. 2012). The broadband reductions shown in the spectra are thus likely linked to broadband changes in the frequency wavenumber spectra of the turbulent fields. A thorough characterisation of the latter is what we aim to do in this study.

Our analysis combines experimental and numerical databases, modal decomposition and locally-parallel, linear mean-flow analysis. The experiments were performed at the Pprime Institute and consisted of Time-Resolved (TR), Stereo PIV measurements at different cross-sections of a jet at Mach number $M_j = 0.9$ subject to a uniform external flight stream at $M_f = 0.15$. Throughout the paper, the database is systematically compared to a case with no flight stream, $M_f = 0$. Companion LES databases were generated for the same operating conditions using the "CharLES" solver by Cascade Technologies (Brès et al. 2017, 2018) in order to obtain a high-fidelity 3D database, allowing us to perform global SPOD.

The remainder of the paper is organised as follows: in §2 we describe the experimental setup and provide details about flow conditions and PIV treatment. This is followed by a description of the numerical setup in §3. In §4 we show the effect of the flight stream on first-order statistics and relevant mean-flow quantities. This part consists in a validation of the two databases with respect to previously reported results. In chapter §5 and §6 the effect of the flight stream is investigated in more depth through Fourier decompositions and local

SPOD. Results of a local, linear mean-flow model are presented in §7 and interpreted in light of the PIV data. Global SPOD analysis using the LES data is discussed in §8 and finally some concluding remarks are given in §9.

2. Experimental setup

The experiments were performed at the *Bruit & Vent* jet facility of the Pprime Institute in Poitiers, France. We performed measurements in jets at Mach number of $M_j = U_j/c_\infty = 0.9$, where U_j is the jet exit velocity and c_∞ the ambient speed of sound. The corresponding Reynolds number was $Re = U_j D/\nu = 1\times10^6$, where ν is the kinematic viscosity and D is the nozzle diameter, which was 50mm. The jet was subject to an external uniform stream which could attain a maximum Mach number of $M_f = U_f/c_\infty = 0.15$, where U_f is its exit velocity. The flight stream comes from an outer convergent section that surrounds the main nozzle and finishes in a straight section of diameter 600mm. The operating conditions in terms of nozzle-pressure ratio are $NPR = P_{t_j}/P_\infty = 1.7$ for the main jet and $NPR = P_{t_f}/P_\infty = 1.006$ for the flight stream, with $P_{t_{j,f}}$ the total pressure and P_∞ the ambient pressure. The experiments were performed in isothermal conditions, the static temperatures of the main jet and the flight stream being controlled to ensure this. The internal and external boundary layers were tripped so as to produce turbulence, similar to what was done in previous studies in static conditions (Brès et al. 2018), at $3D$ upstream of the nozzle exit.

We performed a series of low-frequency-2D and TR-Stereo-PIV measurements. The former were used to characterise the effect of the flight stream in zero and first-order statistics, such as mean-flow distortion and reduction of turbulent kinetic energy, with increasing flight stream Mach number, varying from $M_f = 0$ to $M_f = 0.15$. In the 2D setup, the laser sheet is aligned with the jet axis, allowing a fine discretisation in the streamwise direction. The setup consisted of two Lavision Imager LX cameras and a Quantel Evergreen 532nm, 200mJ laser. The images had a resolution of 4920x3280 pixels, which allowed us to cover an $x-y$ plane in the range $x \in [0.15D, 10D]$ $y \in [-1.9D, 1.9D]$, resulting in one vector every 0.009D. A total of 10000 PIV images were acquired at a rate of 4Hz, which was found to be sufficient to converge mean and rms fields. Both the main jet and the flight stream were seeded with glycerine smoke particles with diameters in the range 1-2μm, similar to what was done in previous PIV campaigns (Jaunet et al. 2017). These experiments were used to characterise velocity statistics with four different flight stream levels corresponding to $M_f = 0, 0.05, 0.1, 0.15$.

The characterisation of different instability mechanisms requires time-resolved flow data decomposed in azimuthal Fourier modes. This was achieved with the Stereo TR-PIV setup, which featured two Photron SAZ cameras and a 532nm, 2x60W continuum Mesa laser. The cameras were positioned in a forward scattering configuration, in order to assure maximal light intensities. The angle formed by the cameras and the laser sheet was 45° (with both cameras on the same side of the laser source), and Scheimpflug adaptors were used to ensure a correct focus on the entirety of the field of view. A resolution of 1024x1024 pixels was used to focus on a field of view in the range $y \in [-1D, 1D]$, $z \in [-1D, 1D]$, resulting in one vector every 0.026D. The image acquisition was performed in double frame mode at a frequency of 10kHz, corresponding to a Strouhal number of $St = 1.6$, giving a total of 21000 images per plane measured. The laser sheet had a thickness of 3mm, and the time between laser pulses was set to 2.5μs, resulting in a maximum displacement of 4 pixels across the laser sheet. For both the 2D and TR-Stereo configurations, PIV computations were carried out using a commercial software which performed a multi-pass iterative PIV algorithm (Scarano 2001). The PIV interrogation area size was set to 64x64 pixels for the first pass, decreased to 16x16 pixels with an overlap of 50 between two neighbouring interrogation areas. Each

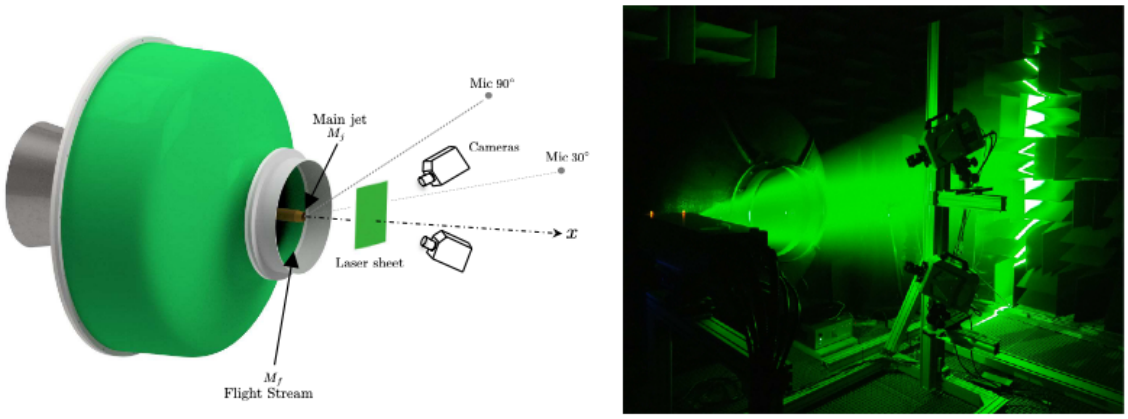

Figure 2: Schematic of the jet facility showing the main elements of the Stereo PIV system, along with a picture of the experiment setup in the wind tunnel.

Case	Re	M_j	M_f	T_j/T_f	2D-PIV	TR-Stereo PIV
1	10^6	0.9	0	1	✓	✓
2	10^6	0.9	0.05	1	✓	-
3	10^6	0.9	0.10	1	✓	-
4	10^6	0.9	0.15	1	✓	✓

Table 1: Operating conditions and experimental parameters of the experiments. The last two columns indicate which kind of PIV setup was used for each condition.

instantaneous snapshot was interpolated into a polar grid, r-θ using a bi-cubic interpolation in order to perform a Fourier decomposition in azimuth (Jaunet et al. 2017). The measurements in the TR-Stereo configuration were carried out for two flight stream conditions, $M_f = 0$ and $M_f = 0.15$, the same used in the numerical databases. Several PIV planes were measured in both conditions at different streamwise stations ranging from $x/x_c = 0.04$ to $x/x_c = 2$, where x_c is the potential core length.

Figure 2 shows a schematic of the jet facility and the TR-PIV setup along with a picture of the setup in the wind tunnel. A summary of the operating conditions of the experiments are shown in Table 1. Acoustic measurements were performed (in the absence of the PIV setup) at polar angles of 30° and 90° to the jet axis, at a distance of 50D from the nozzle. Acoustic data was sampled at a rate of $St_s = 32.7$ for 30s. PSDs reported in figure 1 were computed with Welch's method, using 5860 blocks with 50% overlap. Complementary Pitot tube and hot-wire measurements were performed for case 4 in order to characterise the boundary layers, and are described in more detail in §4.

3. Numerical setup

To complement the experiments, the jet configurations with and without flight stream are investigated with high-fidelity large eddy simulations using the compressible flow solver "CharLES" developed at Cascade Technologies (Brès et al. 2017). Results for the isothermal Mach 0.9 turbulent jet issued from the contoured convergent-straight nozzle of exit diameter $D = 50$mm at $M_f = 0$ were initially reported by Brès et al. (2018). The present work is an

extension of the study for both $M_f = 0$ and 0.15 with longer databases and higher sampling frequency. All the large eddy simulations feature localized adaptive mesh refinement, synthetic turbulence and wall modeling on the internal nozzle surface (and external nozzle surfaces at $M_f = 0.15$) to match the fully turbulent nozzle-exit boundary layers in the experiments. The LES methodologies, numerical setup and comparisons with measurements are described in more details in Brès et al. (2018) and are only briefly summarized here.

3.1. *Setup*

The round nozzle geometry (with exit centered at $(0, 0, 0)$) is explicitly included in the axisymmetric computational domain, which extends from approximately $-10D$ to $50D$ in the streamwise (x) direction and flares in the radial direction from $20D$ to $40D$. The uniform external flight stream is imposed as upstream boundary condition outside the nozzle in the simulation. Note that a very slow coflow at Mach 0.009 is used in the LES at no flight stream condition to prevent any spurious recirculation and facilitate flow entrainment. Sponge layers and damping functions are applied to avoid spurious reflections at the boundary of the computational domain (Freund 1997; Mani 2012). The Vreman (Vreman 2004) sub-grid model is used to account for the physical effects of the unresolved turbulence on the resolved flow.

The nozzle pressure ratio and nozzle temperature ratio are $NPR = P_t/P_f = 1.7$ and $NTR = T_t/T_f = 1.15$, respectively, and match the experimental conditions. The jet is isothermal ($T_j/T_f = 1.0$), and the jet Mach number is $M_j = U_j/c = 0.9$. For both experiment and simulation, the Reynolds number is $Re = \rho_j U_j D/\mu_j \approx 1 \times 10^6$.

In the experiment, transition is forced using an azimuthally homogeneous carborundum strip located approximately $3D$ upstream of the nozzle exit plane on the internal nozzle surface for all configurations, and on the external nozzle surface for $M_f = 0.15$. In the LES, synthetic turbulence boundary conditions are used to model these experimental boundary layer trips present on the internal and external nozzle surfaces. To properly capture the internal and external turbulent boundary layers, localized isotropic mesh refinement and wall modeling (Kawai and Larsson 2012; Bodart and Larsson 2011) are applied on the interior and exterior surface from the boundary layer trip to the nozzle exit. All the other solid surfaces are treated as no-slip adiabatic walls. While several meshes were considered as part of a grid resolution study (Brès et al. 2018), the standard unstructured mesh containing approximately 16 million control volumes is used for the present work with $M_f = 0$, and the case is simply referred to as *BL16M_M09* (i.e., extension of case *BL16M_WM_Turb* from Brès et al. (2018)). For $M_f = 0.15$, the same isotropic near-wall mesh refinement used to capture the boundary layer inside the nozzle is applied outside of the nozzle. The mesh size is therefore increased to approximately 22 million control volumes, and the case is referred to as *BL22M_M09_Mf015*.

Table 2 lists the simulation parameters and settings for the LES runs with and without flight stream, including the time step dt, the total simulation time t_{sim} for the collection of statistics and data (after the initial transient is removed), and the sampling period Δt for the recording for the main LES databases. Note that the sampling period for the recording of the FW-H surface data for far-field noise predictions is $0.5\Delta t$.

To facilitate postprocessing and analysis, the LES data is interpolated from the original unstructured LES grid onto structured cylindrical grids in the jet plume and in the nozzle pipe. These structured cylindrical grids were originally designed for the grid with 16M control volumes, such that the resolution approximately corresponds to the underlying LES resolution. For both structured grids, the points are equally-spaced in the azimuthal direction to enable simple azimuthal decomposition in Fourier space.

Case name	Mesh size	M_j	M_f	T_j/T_f	Re	dtc/D	$\Delta tc/D$	$t_{sim}c/D$
BL16M_M09	15.9×10^6	0.9	0	1.0	1×10^6	0.001	0.1	3000
BL22M_M09_Mf015	21.8×10^6	0.9	0.15	1.0	1×10^6	0.001	0.1	2000

Table 2: Operating conditions and simulation parameters of the main LES, where t_{sim} is the simulation time and Δt is the sampling period of the database recording.

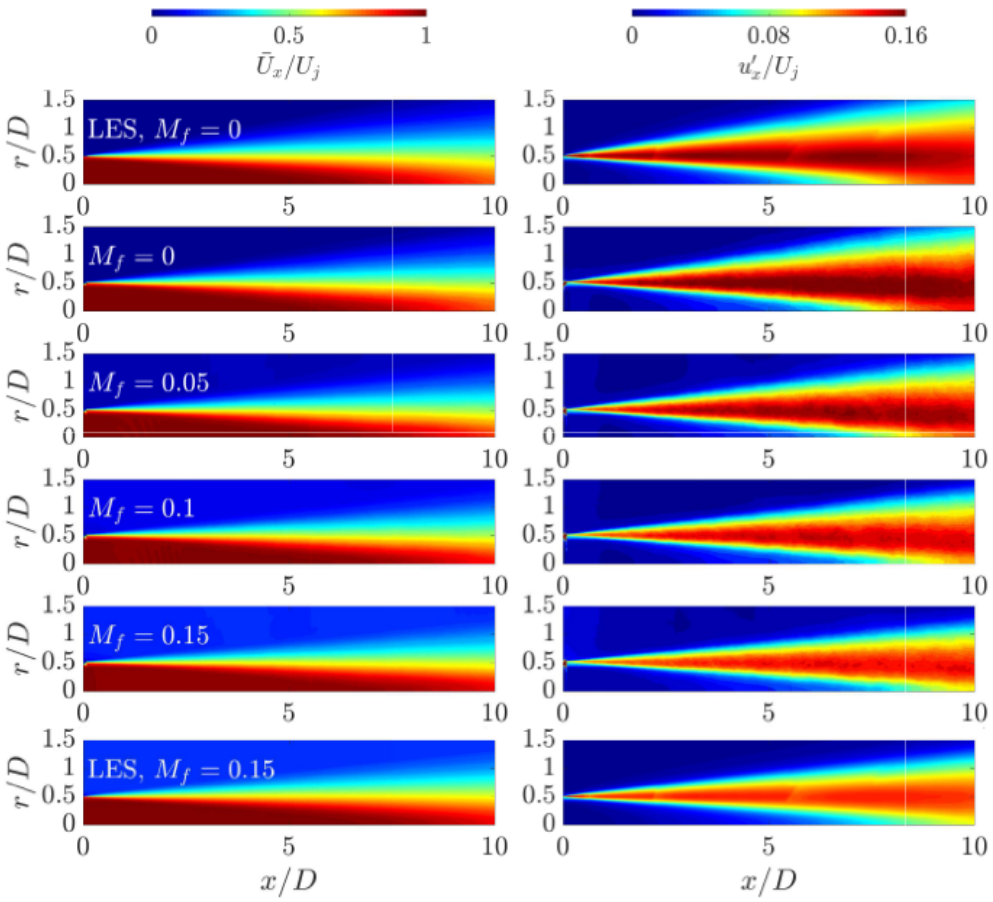

Figure 3: Contours of mean, $\bar{U}_x$ (left), and rms, u'_x (right), streamwise velocity for jets at $M_j = 0.9$ and different flight stream Mach numbers. Velocities are normalised by U_j. The first and last contour maps correspond to LES data, and the intermediary ones to PIV results.

4. Zero- and first-order statistics

We start with an analysis of the effect of the flight stream on zero- and first-order velocity statistics, in order to provide a validation of the experimental and numerical databases. It is known that a flight stream affects the jet development by lengthening the potential core and reducing shear layer spreading and turbulence intensities (Tanna and Morris 1977). These trends can be seen in figure 3, which presents contour plots of mean and rms streamwise velocity on a meridional plane, measured with the 2D-PIV setup, with increasing M_f. LES data for the case $M_j = 0.9$, $M_f = 0.15$ is also shown for comparison.

The LES and experimental databases were found to be in excellent agreement, as can be

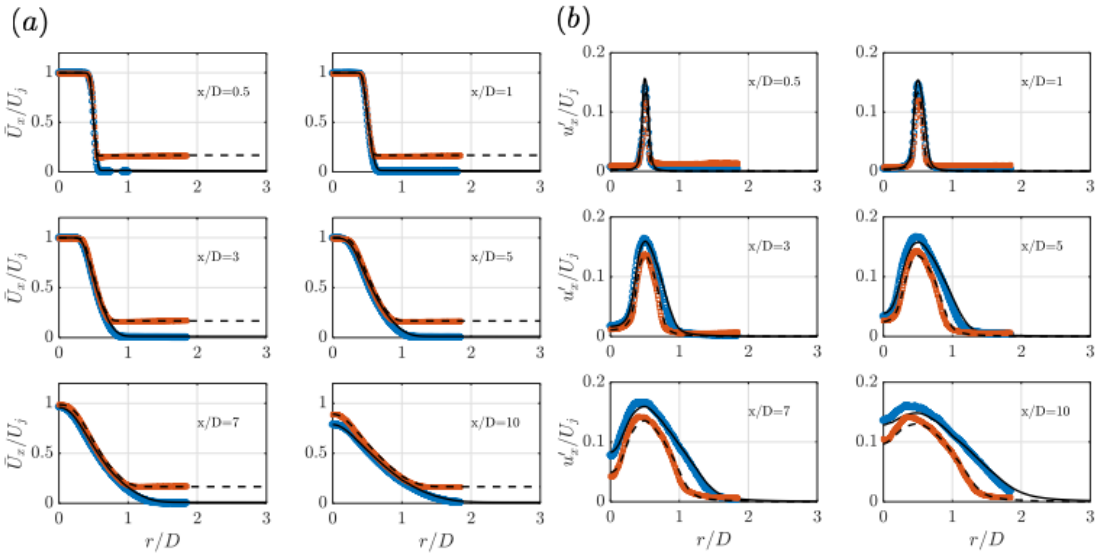

Figure 4: Comparison between experimental and numerical mean(a) and rms(b) radial profiles of streamwise velocity component at different streamwise positions. ○: exp. $M_f = 0$; □ : exp. $M_f = 0.15$; ——:LES data for $M_f = 0$, *BL16M_M09*; - - -: LES data for $M_f = 0.15$, *BL22M_M09_Mf015*.

seen in the radial profiles of mean and rms velocities shown in figure 4 for different streamwise positions. LES data for the no-flight case, *BL16M_M09*, is also shown for comparison. Both jets exhibit a classic change from top-hat profiles in the near-nozzle region to bell-shaped profiles further downstream. However, the reduction in shear-layer thickness becomes apparent after a couple of jet diameters with increasing M_f. The rms profiles measured in the presence of the flight stream show amplitude reductions throughout the jet. These reductions are concentrated in radial positions around the peak in the initial jet region, but spread across the shear layer further downstream.

The mean-flow shape changes with increasing flight stream levels. We assessed three important flow features at different conditions of flight stream Mach number, M_f: the potential core length, x_c, defined here as the streamwise position where $\bar{U}_x(x,0) = 0.95U_j$, the centerline velocity decay and the shear-layer momentum thickness, δ_θ, defined as

$$\delta_\theta(x) = \int_0^{r_{0.05}} \frac{\tilde{U}_x(x,r)}{\tilde{U}_x(x,0)} \left(1 - \frac{\tilde{U}_x(x,r)}{\tilde{U}_x(x,0)}\right) \mathrm{d}r, \tag{4.1}$$

where $\tilde{U}_x$ is a normalised mean flow velocity,

$$\tilde{U}_x(x,r) = \frac{\bar{U}_x(x,r) - U_f}{\bar{U}_x(x,0) - U_f}. \tag{4.2}$$

The evolution of these quantities with increasing M_f is shown in figure 5. The potential core length grows linearly with M_f, presenting an increase of 17% between the no-flight-case and the case with $M_f = 0.15$. The jet development is also affected downstream of the potential core, where the velocity decays at smaller rates in the presence of the flight stream. This delayed development is also manifest in momentum thicknesses, which are significantly reduced. Figures 5(d) and (e) show the evolution of centerline velocity and momentum thickness with the streamwise coordinate scaled by the case-dependent core length x_c. It can be seen that this scaling produces a collapse of the centerline velocity decay. The momentum

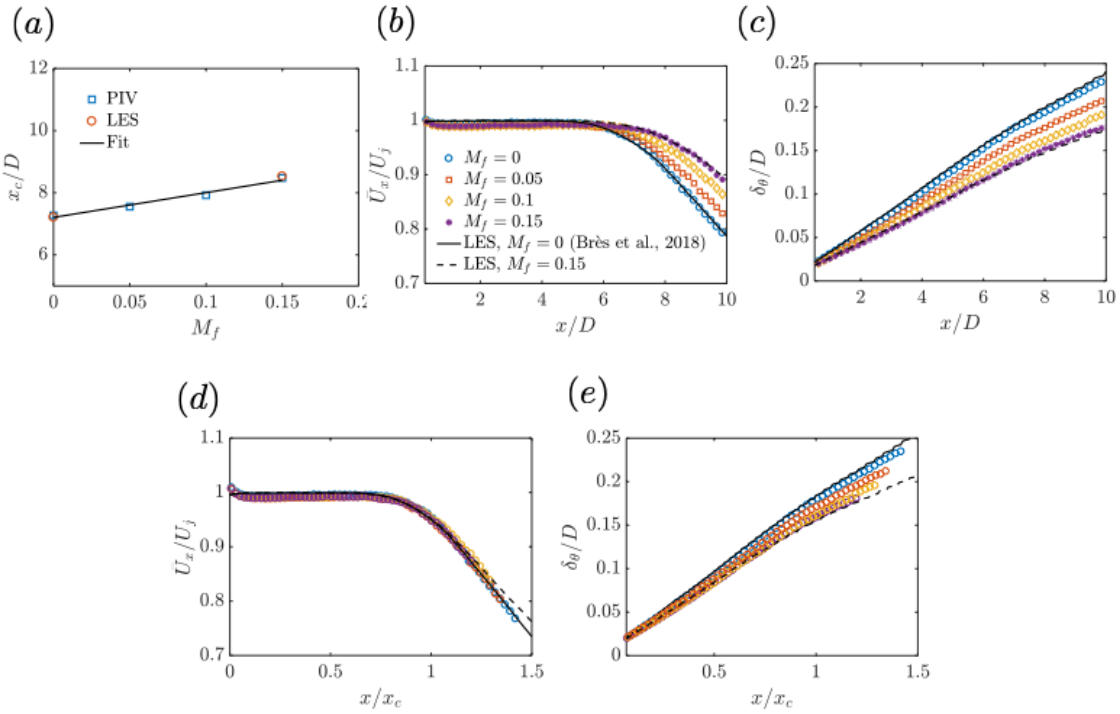

Figure 5: Variation of mean-flow quantities with increasing flight stream velocity for a jet at $M_j = 0.9$. (a) Potential core length; (b) Centerline velocity decay; (c) Streamwise evolution of the momentum thickness. (d) and (e) show centerline velocity and momentum thickness profiles when the streamwise coordinate is scaled by potential core length, x_c. Legends in (c), (d) and (e) are the same as in (b).

thickness, on the other hand, does not collapse so well with this scaling, and the shear-layer remains thinner in the flight case, even when the flow stretching is taken into account.

The boundary layer, which is now recognized as an important flow region underpinning jet dynamics and sound radiation (Brès et al. 2018; Kaplan et al. 2021; Lesshafft et al. 2019) was also characterised through Pitot tube and hot-wire measurements. Figure 6 shows mean and rms profiles for the flight stream case measured at $x/D = 0.0024$, which was the closest position attainable without damaging the probes. The hot-wire had a length of 1.25mm and a diameter of 2.5μ, and the measurements were performed with a 55M01 Dantec anemometer at a frequency of 30kHz ($St = 4.8$). The homogeneity of the boundary layer was verified by measuring the profiles at different azimuthal positions, which were found to be in be in good agreement with each other and the LES profile. Regarding the hot-wire measurements, at $M_j = 0.9$ the *in-situ* calibration of the probes was found to be very problematic, with large errors in the calibration coefficients due to compressibility effects and the large total temperature gradients in the thin initial shear layer. This issue was mitigated by performing the measurements at a lower Mach number, $M_j = 0.7$, for which there was also another LES database available. As shown in figure 6(b), the differences between boundary layer profiles at $M_j = 0.7$ and $M_j = 0.9$ are slight. Rms profiles from the static and flight cases are found to be quite similar in the inner part of the shear layer. In the outer part, $|r/D| > 0.5$, rms values are higher in the presence of the flight stream, as expected. A second peak is seen in the $M_f = 0.15$ profiles at $r/D \approx 0.51$, due to the external boundary layer. The LES profiles are found to be in good agreement with hot-wire data. The peak turbulence intensity and the shape of the curves are consistent with previously investigated turbulent jets.

Overall, the numerical and experimental databases for the jets at $M_j = 0.9$ and $M_f = 0$

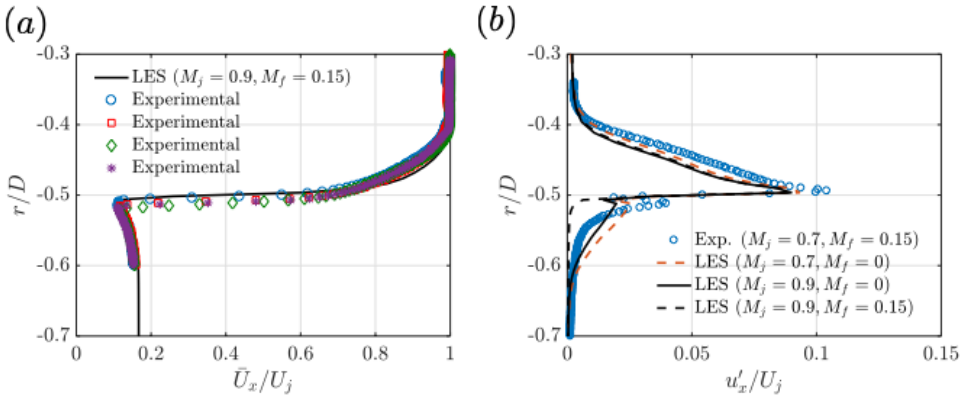

Figure 6: Nozzle-exit mean (a) and rms (b) boundary layer profiles measured in the flight stream case, $M_f = 0.15$. The different experimental profiles in (a) correspond to measurements performed at different azimuthal positions, in order to verify the homogeneity of the boundary layer. Rms profiles for the static case, $M_f = 0$, are shown in (b) for comparison.

are found to be in excellent agreement. Experimental data for the no-flight case, $M_f = 0$, agrees with previously reported data (Brès et al. 2018). Furthermore, the trends in mean flow distortion and rms fields with the flight stream are consistent with data reported in the literature. We now proceed to a more detailed investigation of the effect of the flight stream on structures contained in the turbulent flow, which involves an analysis of energy distribution in the frequency-wavenumber space.

5. Energy distribution across azimuthal modes

We first consider the energy distribution across azimuthal wavenumbers and assess how this is affected by the coflow. This is done by first interpolating the TR-PIV instantaneous fields $u(y, z, t)$ onto a polar grid $u(r, \theta, t)$ and then decomposing them into a Fourier series in θ, obtaining a field $u(r, m, t)$, with m the azimuthal wavenumber (Cavalieri et al. 2013; Jaunet et al. 2017). We then compute the mean square streamwise velocity fluctuations, $u_x'^2(r, m)$, and average them across the shear-layer, resulting in a single value representative of the energy of each m and streamwise position.

We use the potential core length, x_c as a mean-flow scaling parameter. Throughout the remainder of the study we make comparisons between the $M_f = 0$ and $M_f = 0.15$ cases at different streamwise positions on the basis of the normalised coordinate, x/x_c. In previous studies of jets subject to an external flow, attempts have been made to find "stretching factors" that, when used as a suitable scaling to the coordinate system, would make the flow field, the stability characteristics, and turbulent quantities and sound field independent of the external flow velocity. For instance, Michalke and Michel (1979) proposed a scaling factor proportional to the velocity difference which is used to model, with some degree of success, the reduction in SPL produced by the external flow. The factor is calibrated through a fitting procedure of acoustic data. In a similar spirit, Michalke and Hermann (1982) have shown that a scaling can be found that accounts at the same time for the reduction of spatial growth rates of the Kelvin-Helmholtz instability and for the change in the range of unstable frequencies. The scaling factor, however, is wavenumber-dependent. Here we use the potential core length as a physical scaling factor, without delving much further in the search for a "universal" scaling of all aspects of jet dynamics and sound radiation. The suitability of this choice will be discussed in light of the results shown in the following.

Figure 7 shows the distribution of energy for different m at four different positions:

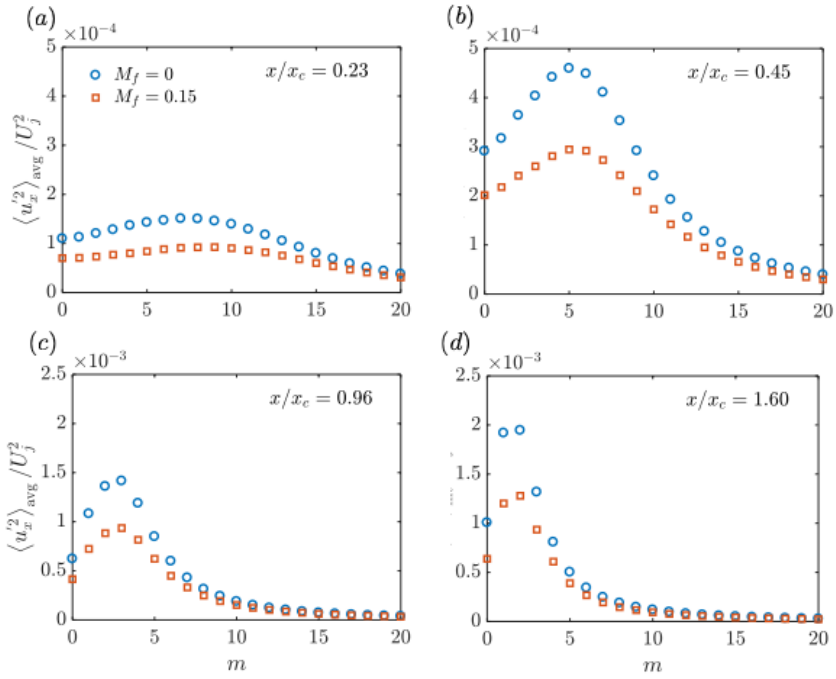

Figure 7: Energy of streamwise velocity fluctuations integrated in r as a function of azimuthal wavenumber, m, for different streamwise positions, x/x_c. Note the change in scale from (a)-(b) to (c)-(d), in order to account for the exponential growth of velocity fluctuations in the streamwise direction.

$x/x_c = 0.23, 0.45, 0.96, 1.6$. At streamwise locations closer to the nozzle exit, the energy distribution is quite broadband, with at least 20 azimuthal modes having significant energy relative to the peak, which occurs around $m = 7{-}8$ at $x/x_c = 0.23$. As one moves downstream, the distribution becomes more narrowband and the energy peak is shifted towards lower m. This is a trend that has also been observed by past experimental (Citriniti and George 2000; Jung et al. 2004; Cavalieri et al. 2013) and numerical studies (Pickering et al. 2020). Figure 7 also reveals that the flight stream produces substantial reductions in energy levels. Closer to the nozzle exit this reduction is seen to be rather broadband, while further downstream the reductions are more concentrated around the energy peak. Overall shape of the spectrum is not significantly altered. However, at the position closest to the nozzle exit, there is a slight shift of the peak towards higher m, and the spectrum is seen to be flatter.

The downstream evolution of the azimuthal wavenumber of the energy peak was also found to be similar, once normalised by x_c, with and without the flight stream, as seen in figure 8. In both cases, the peak evolves towards lower m with downstream position, approximately scaling as $\sim 1/(x/x_c)^n$. The exponent n which provides the best fit with the data was found to be virtually the same for both jets. Far downstream, past the end of the potential core, mode $m = 1$ becomes dominant, in agreement with previous studies Nogueira et al. (2019); Pickering et al. (2020). In the results of figures 7 and 8 can note a subtle difference between near-nozzle and downstream regions. In the former, the peak wavenumber is different, and the spectra are flatter with the flight stream, whereas further downstream the trends are virtually identical for the two jets.

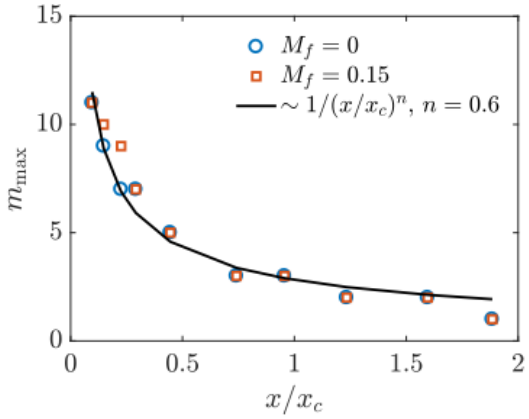

Figure 8: Azimuthal wavenumber of the peak energy as a function of x/x_c. The black and dashed lines are fits of the form $1/(x/x_c)^n$ for the $M_f = 0$ and $M_f = 0.15$, respectively. $n = 0.6$ was found to provide a near-optimal fit for both cases.

6. Frequency-wavenumber energy maps

We now continue the analysis by further decomposing the velocity field into Fourier modes in time. The decomposed velocity field then becomes a function of frequency (Strouhal number), azimuthal wavenumber and radial position, $u_x(St, m, r)$, and we can assess the effect of the flight stream in the frequency-wavenumber plane. Figure 9 shows maps of radially-integrated, power-spectral density of streamwise velocity fluctuations in the $St - m$ plane at the four streamwise positions considered in the previous section. In both flow conditions, the energy peak occurs in the $St \to 0$ limit for azimuthal wavenumbers $m > 0$. Following the downstream development of the jet, the wavenumber associated with the energy peak decreases monotonically, as already revealed in figures 7 and 8, but with the maximum energy always remaining in the $St \to 0$ zone. Downstream of the end of the potential core, mode $m = 1$ eventually becomes dominant, in agreement with previous results (Citriniti and George 2000; Nogueira et al. 2019; Pickering et al. 2020). The flight stream is seen to produce a significant reduction of the energy levels, attenuating the first 15-20 azimuthal wavenumbers. Closer to the nozzle exit, this reduction is seen to take place for a broad range of Strouhal numbers and azimuthal wavenumbers. As the jet evolves downstream, the attenuation gradually becomes concentrated around the energy peak, which occurs at low St.

Analysis of the energy distribution can be complemented by performing a Spectral Proper Orthogonal Decomposition (SPOD). SPOD decomposes the data into an orthogonal basis ranked in terms of an energy norm. This decomposition is instructive for turbulent flows because it acts like a filter for coherent structures: their dynamics are well represented by the leading mode and its modal energy, whereas less energetic modes are usually characterised by incoherent turbulent motion. Leading SPOD modes can then be associated with the Kelvin-Helmholtz, Orr and Lift-up mechanisms, according to their region of dominance in the $St - m$ plane (Nogueira et al. 2019; Pickering et al. 2020). It is important to emphasise, though, that a clear demarcation between the linear mechanisms in the frequency-wavenumber plane does not exist. For example, in the low St range, coherent structures are likely a mixture (for non zero m) of Orr structures, streaks and weak KH wavepackets. Likewise, for the $m = 0$ mode, the transition from KH to Orr-type structures with decreasing St is gradual, with no clear cut. In that sense, the linear maps proposed by Pickering et al. (2020) should not be considered a strict definition, but rather an indication of mechanism dominance, which is nonetheless useful insofar as away from the grey zones the distinction is relatively clear. With that in

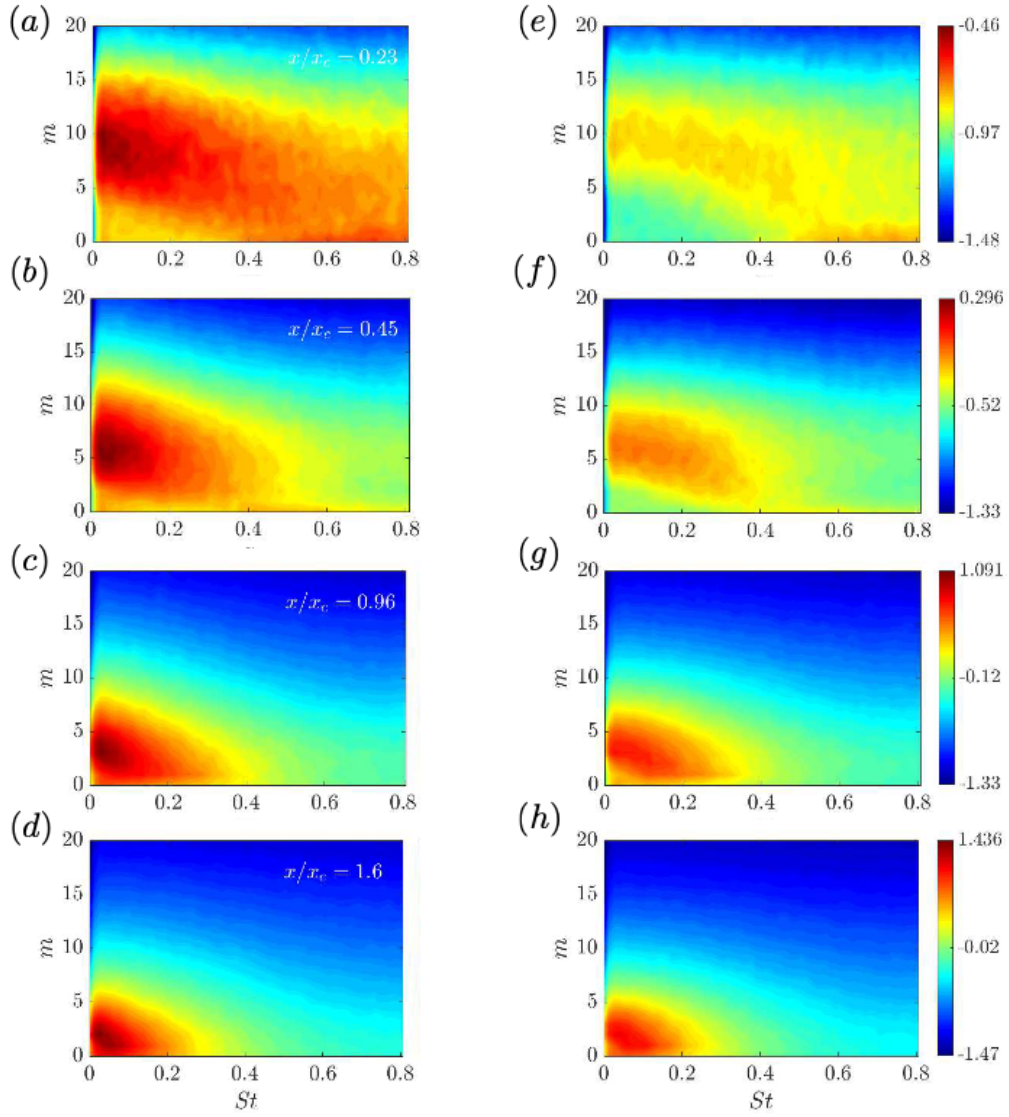

Figure 9: Maps of the radially-integrated PSD of streamwise velocity fluctuations, $\log_{10}(\langle u_x u_x^* \rangle (St, m))$(dB/St) in the frequency-azimuthal wavenumber space for different streamwise positions based on PIV data. (a)-(d): maps for the $M_f = 0$ case; (e)-(h): maps for the $M_f = 0.15$ case. Energy maps for the two cases are shown in the same scale from (a)-(h) at corresponding streamwise positions.

mind, in the following we analyse the modal energy maps of the leading SPOD mode, which in section 7 will be associated with instability mechanisms studied through linear mean-flow analysis.

In the framework of SPOD, given the state vector, $\mathbf{q} = [\rho, u_x, u_r, u_\theta, T]^T$, SPOD modes for a given azimuthal wavenumber and Strouhal number pair, $\mathbf{\Psi}_{m,\omega}$ are obtained through eigendecomposition of the cross-spectral-density (CSD) matrix, $\hat{\mathbf{S}}_{m,\omega}$,

$$\hat{\mathbf{S}}_{m,\omega}\mathbf{W}\mathbf{\Psi}_{m,\omega} = \mathbf{\Psi}_{m,\omega}\mathbf{\Lambda}_{m,\omega}. \tag{6.1}$$

The cross-spectral density matrix is computed as $\hat{\mathbf{S}}_{m,\omega} = \hat{\mathbf{Q}}_{m,\omega}\hat{\mathbf{Q}}^*_{m,\omega}$, where $\hat{\mathbf{Q}}_{m,\omega} = [\hat{\mathbf{q}}^{(1)}_{m,\omega}\hat{\mathbf{q}}^{(2)}_{m,\omega}\cdots\hat{\mathbf{q}}^{(N_{blk})}_{m,\omega}]$ is the ensemble of N_{blk} flow realisations at (m, ω), with $\hat{\mathbf{q}}^{(l)}_{m,\omega_k}$ denoting the lth realisation of the Fourier transforms in time and azimuthal direction at the

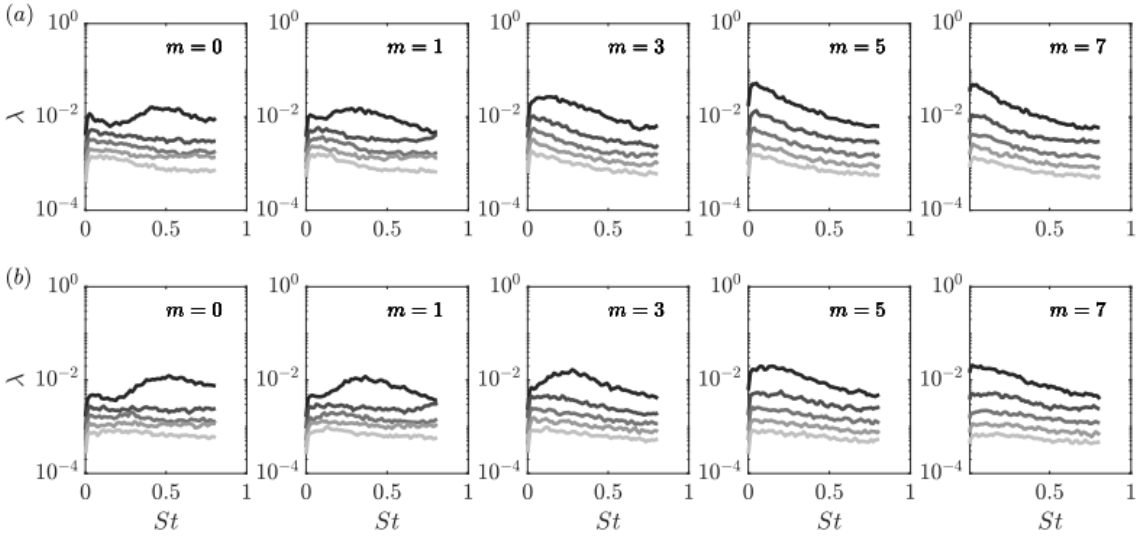

Figure 10: Eigenvalue spectra for the first five SPOD modes computed at $x/x_c = 0.45$ for different azimuthal wavenumbers. Color shading from black to white represent increasing mode numbers (, $\lambda_1 > \lambda_2 > ...\lambda_5$) (a) $M_f = 0$; (b) $M_f = 0.15$.

frequency ω and wavenumber m. The eigenvalues, $[\lambda^{(1)}_{m,\omega}, \lambda^{(2)}_{m,\omega} \cdots \lambda^{nblk}_{m,\omega}]$ corresponding to the modal energy are organised in decreasing order in the diagonal matrix $\mathbf{\Lambda}_{m,\omega}$. The modes so obtained are orthogonal in a given inner product,

$$\langle \mathbf{q}_1, \mathbf{q}_2 \rangle = \mathbf{q}_1^* \mathbf{W} \mathbf{q}_2; \tag{6.2}$$

where $\mathbf{W}$ is a weight matrix containing the numerical quadrature weights and choice of a given norm.

We first consider, using the experimental database, CSDs of different cross-sections of the jet. This "local" approach serves two main purposes: first, it allows us to analyse the evolution of the local organisation with increasing streamwise distance; and second, it allows us to study coherent structures in the initial jet region without their energy being masked by the most energetic structures that dominate the flow far downstream and tend to mask the upstream organisation when viewed using global SPOD. In order to explore the PIV dataset, we reduce the state vector to $\mathbf{q} = [u_x]^T$, and consider a matrix $\mathbf{W}$ that contains trapezoidal quadrature weights for the uniform PIV grid. The CSDs are computed using Welch's periodogram method. For the PIV data, we used blocks of 128 samples and 50% overlap, resulting in a resolution of $\Delta St = 0.0126$. For the LES data, larger blocks of 256 samples were used in order to achieve a resolution similar ($\Delta St = 0.017$) to that of the PIV.

Figures 10 and 11 show eigenvalue spectra of the first five SPOD modes computed at two different streamwise positions $x/x_c = 0.45$ and $x/x_c = 1.6$ for different m. At $x/x_c = 0.45$, a large eigenvalue separation exists between the first and the second modes for the $m = 0$ wavenumber in the range $0.2 \lesssim St \lesssim 0.8$. This separation, which is a signature of the linear KH mechanism, reflects a low-rank behaviour of the jet in the initial region Schmidt et al. (2018); Lesshafft et al. (2019). This large separation disappears for $St \lesssim 0.2$, a region where Orr-like structures become the dominant mechanism in the flow response. The eigenspectra for $m = 1$ display similar trends, although the separation is cut off at $St \approx 0.7$. It can be seen that higher helical modes up to $m = 7$ also display large eigenvalue separation for a broad range of St, with the peak separation shifting to lower St with increasing m.

Further downstream, beyond the end of the potential core, the velocity profiles become

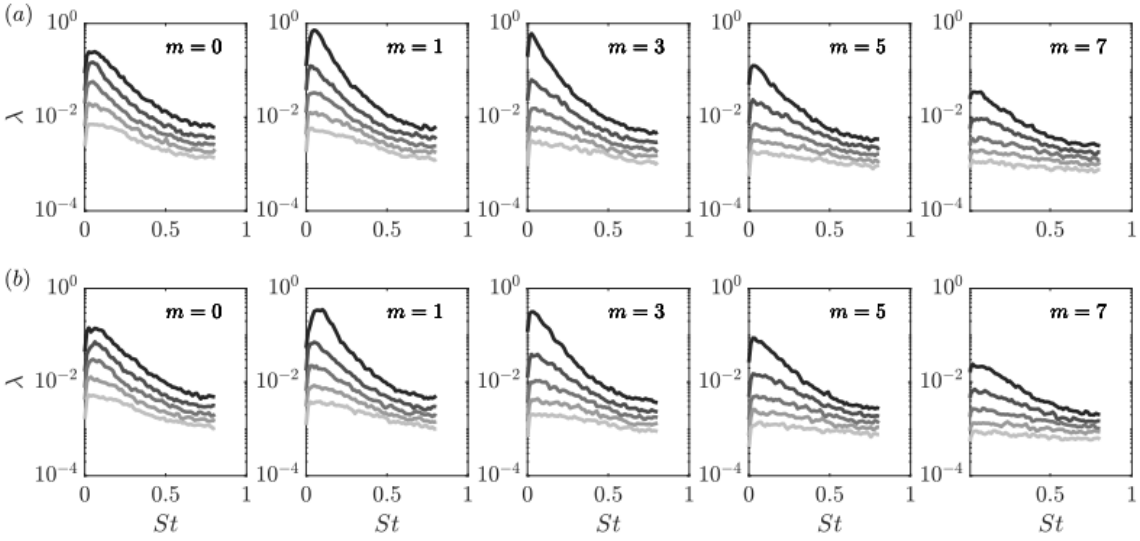

Figure 11: Eigenvalue spectra for the first five SPOD modes computed at $x/x_c = 1.60$ for different azimuthal wavenumbers. Color shading from black to white represent increasing mode numbers (, $\lambda_1 > \lambda_2 > ...\lambda_5$) (a) $M_f = 0$; (b) $M_f = 0.15$.

locally stable, and the associated SPOD eigenvalue separation for the axisymmetric wavenumber disappears. At $x/x_c = 1.6$, the eigenvalue separation for the helical modes decreases sharply with increasing Strouhal, but remains large in the $St \to 0$ limit. In the following, we show modal energy maps of the leading SPOD mode, which we associate with linear instability mechanisms, and infer changes in such mechanisms in the presence of the flight stream. This association is justified in regions of the spectrum where there is a large a separation exists between its modal energy, $\lambda_1(m, St)$, and that of suboptimal modes (even if a precise threshold for low-rank behaviour is unclear). However, we stress that such comparisons such be made with care whenever the leading and suboptimal modes have comparable amplitudes.

Figure 12 shows modal energy maps of the leading SPOD modes, $\lambda_{1_{m,\omega}}$ at the four streamwise positions considered previously. Superposed on these maps are contours of the ratio between the leading and first suboptimal eigenvalues, $\lambda_{1_{m,\omega}}/\lambda_{2_{m,\omega}}$. The modal energy maps follow the same trends as the PSD maps, and also show a striking attenuation with the flight stream. Comparison of figures 9 and 12 reveals that the regions of large eigenvalue separation, $\lambda_{1_{m,\omega}}/\lambda_{2_{m,\omega}}$, overlap, to a great extent, with regions of high energy in the spectrum. Besides the energy attenuations, the flight stream also produces a significant effect on the eigenvalue separation. Close to the nozzle exit, $\lambda_{1_{m,\omega}}/\lambda_{2_{m,\omega}}$ is reduced for almost all the azimuthal wavenumbers in the range $St \gtrsim 0.2$. As the jet evolves downstream, this decrease in eigenvalue separation gets gradually concentrated at lower St and lower m, following the shift in energy peak. This implies that the energy attenuation is accompanied by a weakening of the leading SPOD modes which describe the most energetic, and often also the most coherent, flow structures. These have been shown to be associated with modal and non-modal linear instability mechanisms (Nogueira et al. 2019; Pickering et al. 2020). In the initial jet region, modal growth mechanisms are strong, with KH wavepackets being convectively unstable for a broad range of frequencies starting from $St \gtrapprox 0.1$ and azimuthal wavenumbers $m < 5$, as will be shown shortly by the linear mean-flow analysis. Non-modal mechanisms, which dominate the energy spectrum throughout the jet, give rise to Orr ($m = 0$) streaky ($m > 0$) structures, and have peak energy in the $St \to 0$ limit. The modal maps shown here suggest an attenuation of these three mechanisms, as revealed by both the energy

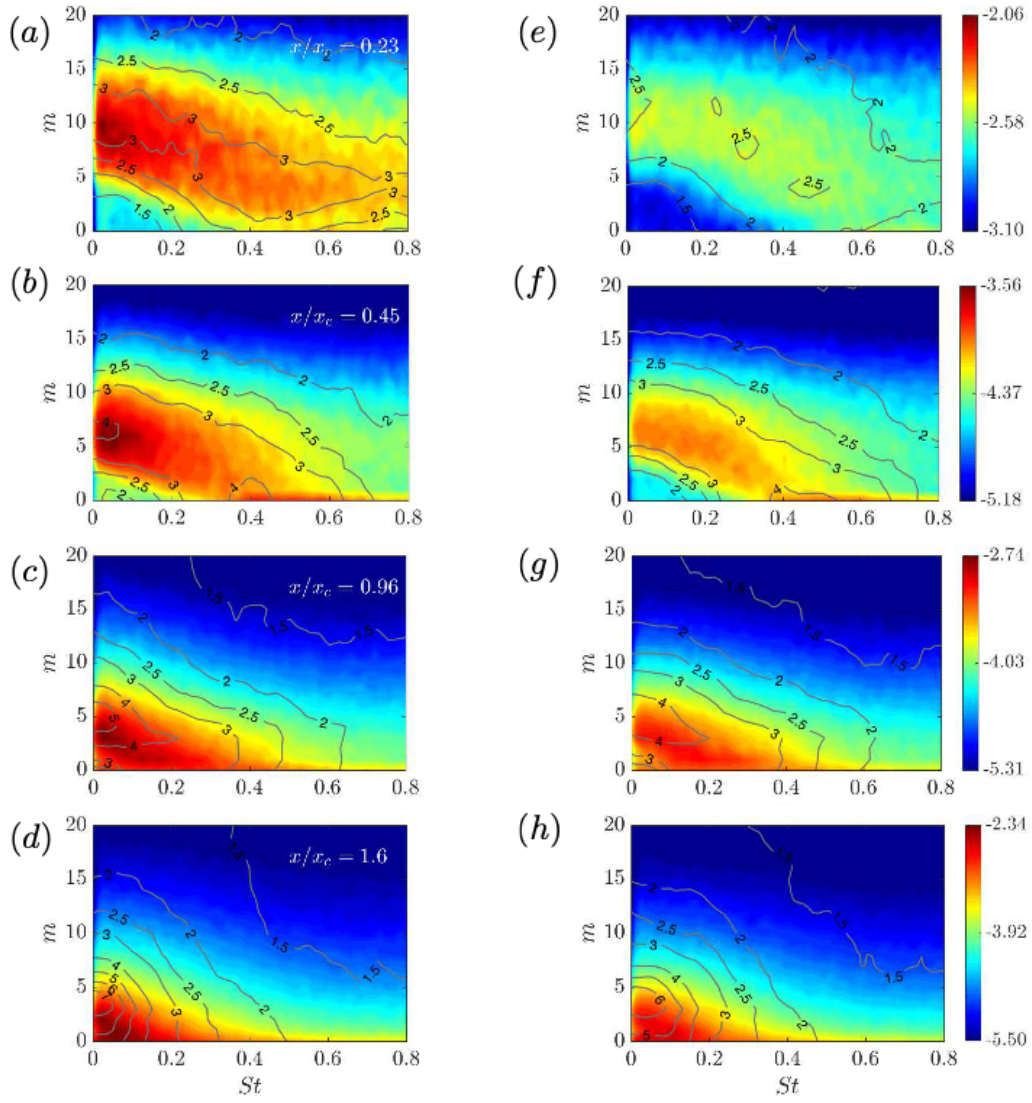

Figure 12: Modal energy maps obtained through SPOD of PIV data. (a)-(d): maps for the $M_f = 0$ case; (e)-(h): maps for the $M_f = 0.15$ case. Colormaps correspond to the leading eigenvalue, $\log_{10}(\lambda_{1_{St,m}})$. Gray contours represent values of the ratio between the leading and first suboptimal eigenvalues, $\lambda_{1_{m,\omega}}/\lambda_{2_{m,\omega}}$

reduction and the lower eigenvalue separation. As mentioned above, in regions where the leading and suboptimal modes have comparable amplitudes, the distinction between different instability mechanisms in the data is muddier, and the leading SPOD mode probably displays combined characteristics of different mechanisms. This is the case, for instance, at the lower left corner of the energy maps in the initial jet region, (figures 12(a),(e),(b),(f)). That part of the $St - m$ spectrum is the same that Pickering et al. (2020) showed to be underpinned by an interplay between streaks, Orr structures and weak KH wavepackets.

Apart from the overall reduction in levels, it is also interesting to assess whether the flight stream changes the energy distribution in the $St - m$ plane. Figure 13 shows modal energy maps normalised by their maxima. The normalisation reveals that, for a given m, the spectrum is much broader in the St direction with the flight stream, especially upstream of the end of the potential core. Whereas in the $M_f = 0$ case the peak in the spectrum is concentrated in the$St \to 0$ region, for the $M_f = 0.15$ case it flattens and spreads to higher St.

The same trends were found in normalised PSD maps (not shown). Interestingly, for a given St, the azimuthal organisation is less affected by the flight. This can be illustrated by the normalisation proposed by Pickering et al. (2020), where the modal energy at each (St, m) pair is divided by the sum of energy across all wavenumbers, $\sum_m \lambda_1(m, St)$,

$$\tilde{\lambda_1} = \lambda_1(m, St) / \sum_m \lambda_1(m, St). \tag{6.3}$$

This metric, shown in figure 14, provides a more direct indication of the most energetic azimuthal wavenumber at each St. Close to the nozzle exit, helical modes (underpinned by the lift-up mechanism) are clearly dominant. As the jet evolves downstream, $m = 0$ Kelvin-Helmholtz wavepackets grow exponentially and dominate the spectrum at $St \geqslant 0.4$. This is seen here more clearly than in figure 12. Further downstream, mode $m = 1$ becomes important in a broad range of Strouhal numbers, and the Orr mechanism also starts to leave its signature at low Strouhal numbers. However, in the limit $St \to 0$, the streak mechanism ($m > 0$) is always the dominant one. When normalised this way, the energy maps for the two jets were found to display a very similar organisation over an extensive streamwise range. At the very initial jet region, represented here by the plots at $x/x_c = 0.23$, it can be seen, however, that the $M_f = 0.15$ case has a broader spectrum the m direction. But the discrepancy with respect to the baseline case diminishes with increasing streamwise distance, and the maps for both jets are globally very much alike.

The results presented in sections §4-6 provide a comprehensive view of the effect of the flight stream, starting from zero-th order statistics, down to a more detailed analysis, through successive Fourier and modal decompositions, of how these changes are arranged in the frequency-wavenumber spectrum, and how they affect the most energetic and coherent structures at different streamwise positions. Comparisons between the streamwise evolution of jets with and without the flight stream on the basis of the normalised coordinate, x/x_c, produce an interesting similarity in certain properties of the flow between the flight and static cases. For instance, the centerline velocity profiles for different flight stream velocities collapse when the normalisation is applied. The azimuthal organisation of energy for the two jets are also found to be in good agreement for equal x/x_c. The shape of the spectra are quite similar, as shown in figures 7 and 14. Furthermore, the most energetic azimuthal modes, $m_{\max}(x/x_c)$ are also very similar, decaying exponentially with increasing x/x_c at a rate which is virtually the same in the flight and static cases. However, as mentioned above, slight discrepancies occur in the near-nozzle region, where the azimuthal spectra for the flight case are flatter and the peak is shifted towards higher m. Interestingly, it is in the same region that the eigenvalue separation, $\lambda_{1_{m,\omega}}/\lambda_{2_{m,\omega}}$ is significantly reduced by the flight stream. This indicates a reorganisation of the flow in which energy is carried by somewhat more "disorderly" motion at higher m at the expense of the most coherent structures associated with the leading SPOD mode.

On the other hand, other flow properties scale less well with x_c. For instance, good collapse of the momentum thickness as a function of x/x_c was not observed. Normalised modal maps, $(\lambda_{1_{St,m}}/\max(\lambda_{1_{St,m}}))$ for two jets were also found to be quite different, with the flight stream producing spectra which are broader in the St direction at a given x/x_c. This behaviour is more pronounced in the initial jet region. As will be explained in the next section, these two trends are connected. The slower growth of the shear-layer leads to a broader range of unstable frequencies, which in turn generates the broader spectrum.

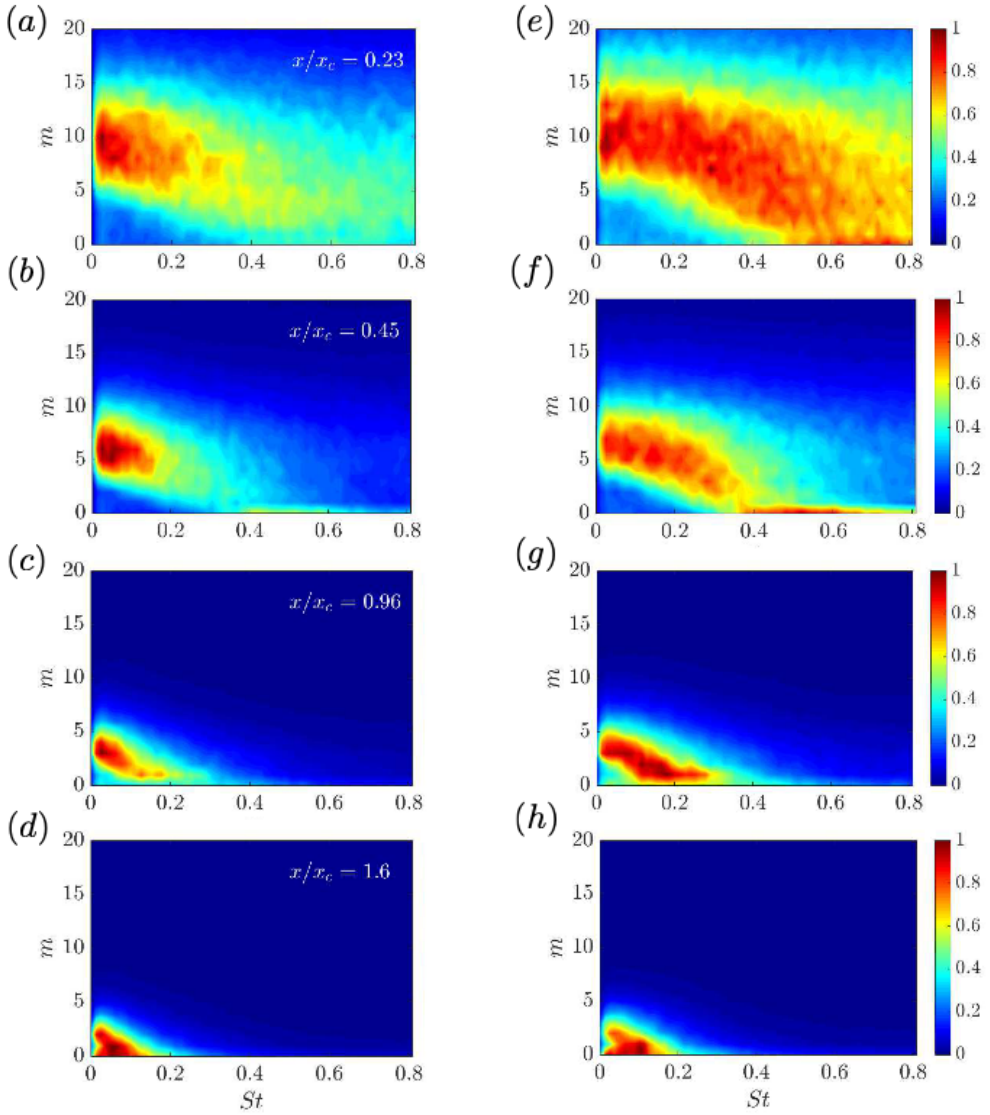

Figure 13: Normalised modal energy maps of the leading SPOD mode, $(\lambda_{1_{St,m}}/\max(\lambda_{1_{St,m}}))$ in the frequency-azimuthal wavenumber space for different streamwise positions based on PIV data. (a)-(d): maps for the $M_f = 0$ case; (e)-(h): maps for the $M_f = 0.15$ case.

7. Linear mean-flow analysis

The results reported above raise the question as to what causes the observed energy attenuation. Is it simply a mean-flow modification effect (and in this case it is something that can be mimicked through a linear model), or is it rather due to a deeper (nonlinear) reorganisation of turbulence? We address this issue through a locally-parallel linear model, where linearisation is performed about the mean flow. The analysis starts with the linearised Navier-Stokes equations written in an input-output form:

$$\frac{\partial \mathbf{q}'}{\partial t} + \mathcal{A}_{\bar{\mathbf{q}}}\mathbf{q}' = \mathbf{f}, \tag{7.1}$$

where $\mathbf{q}'$ is a vector containing fluctuations (in a Reynolds-decomposition sense) of the state variables and $\mathcal{A}_{\bar{\mathbf{q}}}$ is the linearised Navier-Stokes operator. The subscript $_{\bar{\mathbf{q}}}$ denotes linearisation about the mean flow. $\mathbf{f}$ is a term representing the nonlinear Reynolds stresses,

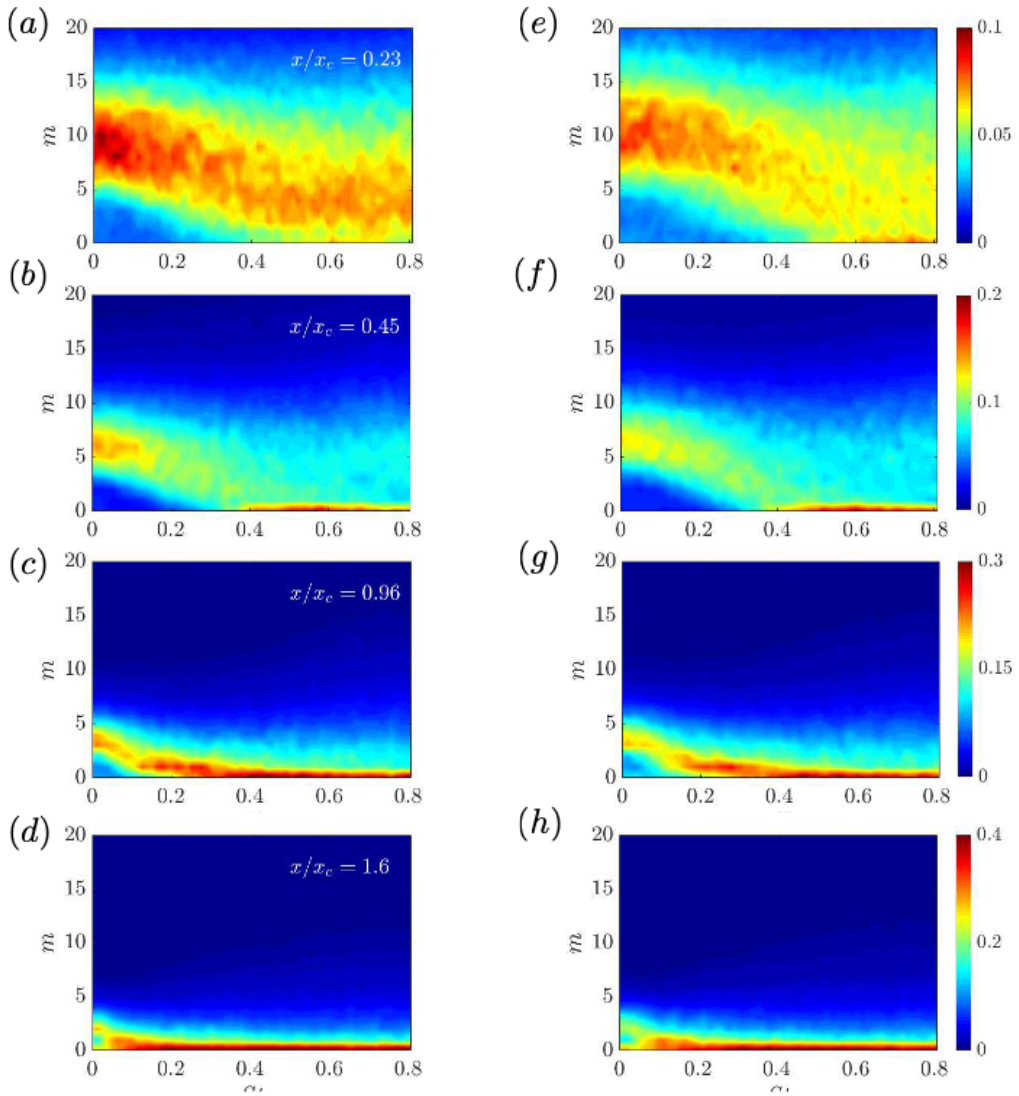

Figure 14: Modal energy maps of the leading SPOD mode in the $St - m$ plane for different streamwise positions based on PIV data. Modal energy is normalised by the sum of energy across azimuthal modes $\sum_m \lambda_1(m, St)$ for each Strouhal number. (a)-(d): maps for the $M_f = 0$ case; (e)-(h): maps for the $M_f = 0.15$ case.

which are treated as an endogenous forcing term. In the locally-parallel framework, we assume flow perturbations of the form,

$$\mathbf{q}'(x, r, \theta, t) = \hat{\mathbf{q}}(r)\exp^{i(\alpha x - \omega t + m\theta)}, \tag{7.2}$$

where the radial structure of the perturbations is given by $\hat{\mathbf{q}}(r)$, α and m are streamwise and azimuthal wavenumbers, respectively, and ω is the frequency. Applying a Fourier transform in 7.1 and substituting the *Ansatz* in 7.2, yields

$$-i\omega\hat{\mathbf{q}} + (\mathcal{A}_0 + \alpha\mathcal{A}_1 + \alpha^2\mathcal{A}_2)_{\bar{\mathbf{q}}}\hat{\mathbf{q}} = \hat{\mathbf{f}}, \tag{7.3}$$

where the linear operators $\mathcal{A}_0, \mathcal{A}_1$, and $\mathcal{A}_2$ contain terms issuing from zero-th, first and second order derivatives in x, respectively. The superscripts $\hat{}$ denote Fourier transformed quantities. Details about the linearisation procedure, the operators and the boundary conditions are given in Appendix §A.

We carried out the analysis in the initial jet region. The mean flow profiles that served as input to the model were based on experimental data, and fitted with the hyperbolic tangent profiles proposed by Michalke and Hermann (1982). At frequencies for which the flow experiences a strong modal convective instability, it is know that eigenanalysis based on a spatial stability formulation provides a suitable framework to describe coherent structures in jets (Jordan and Colonius 2013). When the modal instability is weak other approaches should be used to study linear mechanisms. We address such cases with a model based on the response modes of the resolvent operator. Since the work of McKeon and Sharma (2010), resolvent analysis has been extensively used to identify optimal forcing and response mechanisms in laminar and turbulent flows and to model observed coherent structures.

7.1. *Eigenanalysis: spatial stability*

In eigenanalysis, the nonlinear forcing terms are assumed negligible. The linearised Navier-Stokes system can then be recast in the form of an eigenvalue problem. We here consider the spatial stability problem, for which the eigenvalue problem is given by,

$$\mathbf{L}\hat{\mathbf{q}} = \alpha\mathbf{F}\hat{\mathbf{q}}, \tag{7.4}$$

where $L = -\omega\mathbf{I}+\mathcal{A}_0$ and $F = -\mathcal{A}_1$. For high Reynolds numbers such as those considered here, Rodríguez et al. (2015) have shown that α^2 viscous terms can be neglected. The streamwise evolution of disturbances is governed by the sign of the imaginary part of the waveumber, α_i. If $\alpha_i < 0$, disturbances grow exponentially in the positive x direction. In the following, we analyse the behaviour of the most unstable mode given by 7.4, which corresponds to the Kelvin-Helmholtz instability. Figure 15 shows contours of α_i in the $St - m$ plane for instability analyses performed at $x/x_c = 0.23$. A region of strong convective instability is seen for $m = 0$-4 on a broad range of Strouhal numbers. Higher azimuthal wavenumbers were found to be stable for all Strouhal numbers analysed. As the jet evolves downstream, the region of convective instability gradually shifts to lower frequencies (not shown), following the thickening of the shear-layer. This is followed by a reduction of growth rates and eventual stabilization of the Kelvin-Helmholtz mode, as will be shown shortly; therefore, the $St \to 0$ region is always characterised by low growth rates. We note two important changes in the instability contours with the flight effect: a shift of the peak α_i to higher St and a broader range of unstable frequencies. These changes are associated with the fact that the shear-layer thickness evolves at different rates for the two jets. As shown in figure 5, normalising the streamwise coordinate by x_c corrects some of the discrepancy but does not eliminate it entirely, and the shear-layer in the $M_f = 0$ still grows at a faster rate; therefore, for the same x/x_c, the jet with the flight stream has a smaller δ_θ. The thinner shear layer causes the most amplified mode to occur at a higher frequency, and the range of unstable frequencies to be broader. The broader range of amplified disturbances in turn offers more possibilities for nonlinear interactions between those disturbances to occur. This may explain why the flight stream produces a broader spectrum in the near-nozzle region, as seen in figure 13.

These changes are followed by a decrease in the peak growth rates, as can be more clearly seen in figure 16 for the $m = 0$ and $m = 1$ azimuthal modes. In order to correct the discrepancy, Michalke and Hermann (1982) proposed a scaling of the growth rates and frequencies by a "stretching factor", derived from similarity considerations, $A = 1 + \Delta U/c_n U_f$, where $\Delta U = U_j - U_f$ and c_n is a neutral phase velocity (we have adapted their variable nomenclature to avoid confusion with ours). This scaling was found to provide a reasonable match for the modified growth rates, $\alpha_i\delta_\theta A$ and frequencies, $\omega\delta_\theta/(\Delta U A)$ for jets in static and flight conditions. However, the stretching factor is not universal, but a function of m and δ_θ. Furthermore, the match worsens with increasing shear-layer thickness, due to deviations from

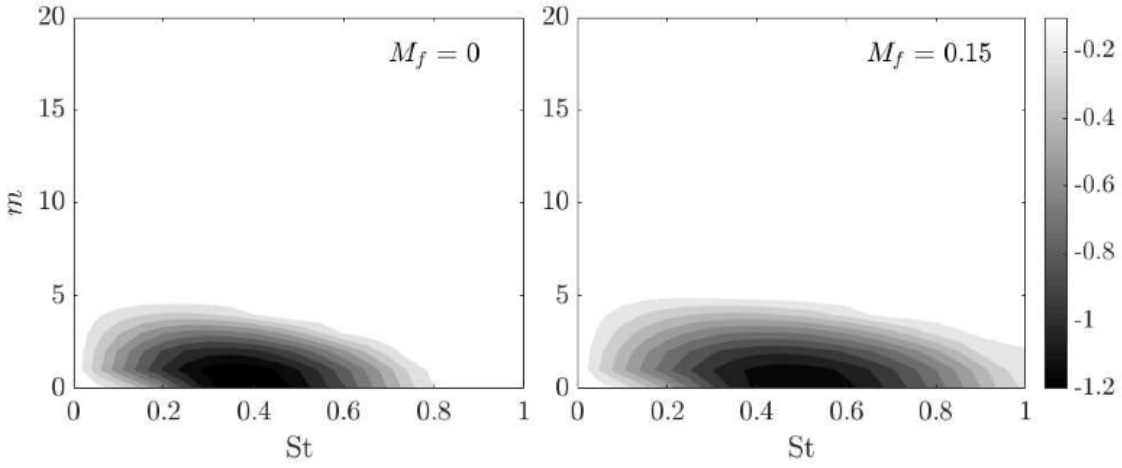

Figure 15: Contours of the growth rates, α_i, of the Kelvin-Helmholtz mode in the $St - m$ plane, computed at $x/x_c = 0.23$.

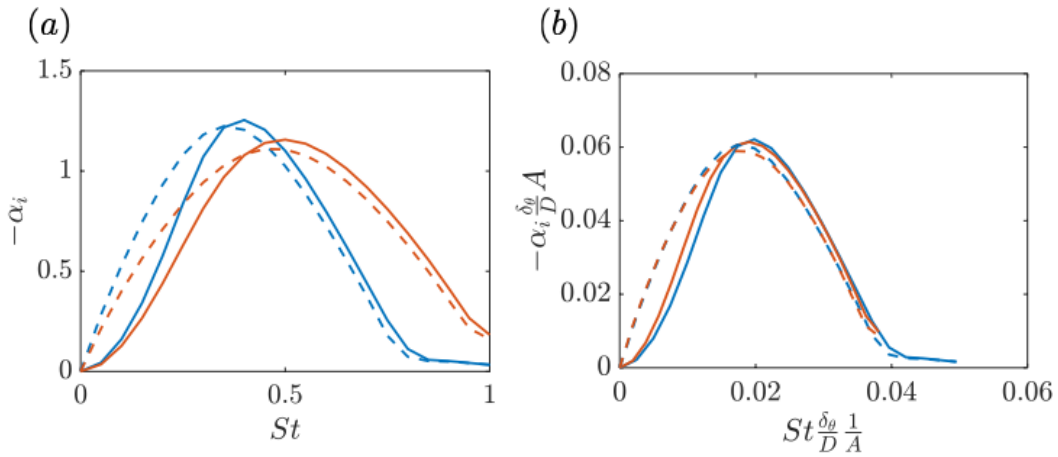

Figure 16: Growth rates of the Kelvin-Helmholtz instability for azimuthal modes $m = 0$ and $m = 1$ at $x/x_c = 0.23$. In (a), as a function of Strouhal number. In (b), the Strouhal number and growth rates are normalised using the local momentum thickness, δ_θ/D, and a stretching factor, A, which we define as the ratio between the potential core lengths in the flight and static cases. ——: $m = 0$, $M_f = 0$; - - -: $m = 1$, $M_f = 0$; ——: $m = 0$, $M_f = 0.15$; - - -: $m = 1$, $M_f = 0.15$.

the hypotheses made in the derivation. Here we propose a scaling with a fixed stretching factor, given simply by the ratio between potential core lengths, $F = (x_c)_f / (x_c)_s$, where the subscripts f and s refer to the static and flight cases, respectively. The modified growth rates and Strouhal numbers are thus given as $-\alpha_i \frac{\delta_\theta}{D} A$ and $St \frac{\delta_\theta}{D} \frac{1}{A}$. Figure 16(b) shows that the scaled curves are in excellent agreement, both in the frequency of the peak and its magnitude. Similar agreements were found for other x/x_c in the initial jet region. Figure 17 shows the streamwise evolution of the Strouhal number of the most amplified mode for the $m = 0$ wavenumber. When corrected by the stretching parameters, the peak Strouhal numbers, $St_{max} \frac{\delta_\theta}{D} \frac{1}{A}$, are found to be virtually the same for two jets, and to be nearly independent of streamwise position. This scaling shows therefore that the frequency shift of the most unstable wavenumber is related to the shift in the potential core length.

Figure 18 shows the streamwise evolution of the axisymmetric KH growth rates for four